Single-spin wavy brim bucket hat in the band edge of monolayer GdIH

Ningning Jia,[1] Zhao Yang,[1] Jiangtao Cai [●],[2] Zhiheng Lv,[1] Yongting Shi,[1] Tielei Song [●],[1] Xin Cui,[1] and Zhifeng Liu [●][1,*]

[1]*Key Laboratory of Nanoscience and Nanotechnology, School of Physical Science and Technology, Inner Mongolia University, Hohhot 010021, China*

[2]*School of Physics and Information Science, Shaanxi University of Science and Technology, Xi'an 710021, China*

Exotic electronic bands, such as flat, linear crossing, and spontaneous valley- or spin-polarized bands, in two-dimensional materials have been a hot topic in condensed-matter physics. In this paper, we first proposed a general dispersion model for possible hatlike electronic bands. Then, we identified a single-spin *wavy brim bucket hat* in the valence-band edge of a stable ferromagnetic semiconducting electrene, the Janus GdIH monolayer, which can be well described by a simplified two-band Hamiltonian model. Specifically, the hat band exhibited a wavy brim with six valleys along the boundary of the first Brillouin zone and held a flat top close to the Fermi level. This resulted in the emergence of single-spin van Hove singularity divergence and Lifshitz transitions. Due to the breaking of both time-reversal and space-inversion symmetries, a sizable spontaneous valley polarization was observed between adjacent brim valleys. This provided the opportunity to realize the high-temperature anomalous valley Hall effect. Particularly, via modest strains and carrier doping, various conductive bipolar states (spin-up versus spin-down, K valley versus −K valley, and ultra-low-speed versus ultra-high-speed) can be modulated from the distorted wavy brim bucket hat of GdIH monolayer.

I. INTRODUCTION

In condensed-matter physics, the electronic behavior of solid-state materials has always been a central topic [1]. The band theory states that the electronic properties of a crystal depend mainly on its band structure [2,3], especially its valence or conduction edges in the vicinity of the Fermi energy. Over the past few decades, many exotic frontier bands, such as flat [4], linear Dirac/Weyl [5,6], half-metallic [7], and ferrovalley bands [8], have been identified with excellent features and promising applications. The discovery of a new distinguished band often triggers new physics, applications, and manufacturing chains.

Bloch electrons in periodic crystals have three intrinsic degrees of freedom: charge, spin, and valley (the local minimum or maximum of the band edges). Their utilization places special requirements on electronic bands, and gives birth to different subdisciplines, corresponding to microelectronics [9], spintronics [10], and valleytronics [11]. As a major factor, band dispersion determines the movement behavior of charge carriers in crystals. Generally, the effective mass m^*, defined as $\hbar^2/m^* = d^2E(\boldsymbol{k})/d\boldsymbol{k}^2$, is a key parameter that reflects band dispersion and can assume three cases: $m^* = C$ (a finite constant), $m^* \to 0$, and $m^* \to \infty$. For the latter two extremes, the local band dispersions should be linear and flat, respectively, and they have attracted considerable attention in the past few decades [4–6]. To date, linear Dirac/Weyl dispersions have been widely identified in topological insulators [12] and semimetals [5], and dispersionless flat/quasiflat

states have been detected in the kagome lattice [13], moiré superlattice [14], and many other lattices (e.g., pyrochlore, Lieb, and bipartite) [4].

As the electron spins can be used as information carriers, spin transport electronics is considered to be a promising methodology for increasing the efficiency of data storage and transfer in next-generation information technology [10]. One of the major challenges in practical applications of spintronics is the generation or injection of spins into real materials [6]. In this context, intrinsic ferromagnetic materials with high or even 100% spin polarization are highly desirable. In solid bands, a significant lifting of spin degeneracy is usually induced by magnetic exchange interactions. Based on the different features of band dispersion, various fully spin-polarized bands have been proposed to meet different spin transport requirements and physical applications, such as half-Dirac [15], spin-gapless semiconducting [16], single-spin flat [17], and bipolar magnetic semiconducting bands [18].

As an analog of spin, valley (termed as pseudospin) can also be employed to store and transmit information. This is due to the existence of a large separation between inequivalent valleys in momentum space and strongly suppressed intervalley scattering [19]. In valleytronics, similar to spintronics, generating valley polarization is a significant challenge. Some external strategies (e.g., optical pumping [20], magnetic doping [21], magnetic proximity [22], external magnetic fields [23], and electric fields [24]) have been experimentally confirmed to be effective in eliminating valley degeneracies. However, many insurmountable drawbacks (e.g., limited carrier lifetimes, the clustering effect, enlarged device size, and weak valley polarization) still exist [25]. These drawbacks have greatly hampered the development of valleytronics.

*Contact author: zfliu@imu.edu.cn

Facing such a challenge, in 2016, Tong *et al.* proposed a ferrovalley band with an intrinsic spontaneous valley polarization, which may open a new avenue for valleytronics. For extreme band dispersions, half-valley metal [26] or valley-half semimetal [27] states with linear Dirac bands have been established to realize valley-dependent ultra-high-speed quantum transport.

In the aforementioned exotic bands, researchers usually focus only on a certain aspect related to the degrees of freedom of Bloch electrons. However, to miniaturize the next-generation electronic devices, integrating and manipulating multiple functions in a single nanomaterial is necessary. Therefore, realizing the combination and flexibility of charge, spin, valley, and extreme dispersion in a single band would be exciting. In this study, we established a general dispersion model for possible hatlike bands and subsequently demonstrated the novel hatlike dispersion to meet the above expectations. We termed the hatlike dispersion a *wavy brim bucket hat*, which can be derived from a simple two-band Hamiltonian model. Using first-principles calculations, we showed a ferromagnetic two-dimensional (2D) electrene Janus GdIH monolayer (ML) to harbor a single-spin wavy brim bucket hat at its valence-band edge. Moreover, the structure, stability, and magnetic properties of the GdIH ML were systematically investigated. In particular, the possible new physics and potential applications of the single-spin wavy brim bucket hat band are discussed in this paper.

II. COMPUTATIONAL METHODS

In our first-principles calculations, all geometric optimizations and electronic structure calculations were performed within the density functional theory (DFT) framework using the Vienna *ab initio* simulation package (VASP) [28]. The generalized gradient approximation (GGA) of the Perdew-Burke-Ernzerhof (PBE) functional was adopted to address the exchange-correlation interactions [29]. A plane-wave basis with a cutoff energy of 600 eV was employed to expand the wave functions. A Monkhorst-Pack k-point mesh [30] with a uniform spacing of $18 \times 18 \times 1$ was used to sample the Brillouin zone (BZ). During the structural relaxation, the convergence criteria of total energy and residual Hellmann-Feynman force on each atom were set to 10^{-6} eV and 0.001 eV/Å^{-1}, respectively. To avoid interactions between adjacent periodic images, a large vacuum space of 20 Å was applied along the z-direction. Considering the correlation effect, we adopted the GGA + U method with $U = 4.6$ eV for the valence electrons in the $4f$ orbital of Gd atoms, which has also been used in other Gd-related systems [31]. Additionally, calculations using the hybrid functional method (HSE06) [32] were conducted to assess the reliability of the electronic band structure obtained from GGA + U. The Berry curvature was calculated using the VASPBERRY code [33] and the Fukui method [34].

III. RESULTS AND DISCUSSION

A. General dispersion model for different hatlike bands

In the past two decades, a Mexican-hat-shaped curious band dispersion [35] has been found in some 2D materials

(e.g., bilayer graphene [36,37], III-V Ga$_2$X$_2$ ML [38], and penta-graphene [39]), and it has been experimentally confirmed in GaSe ML [40]. Due to the existence of 1D van Hove singularities (VHS) in the density of states (DOS) [41], such 2D materials have proven promising for multiferroics [41], magnetism [42], thermoelectronics [43], and scaled transistors [44].

Inspired by the reported Mexican hat bands and based on 3D surface geometrics [35–41], we first proposed a general dispersion model, which should be universal for describing possible hatlike bands in 2D systems. The specific expression can be written as a trigonometric polynomial,

$$E(k_x, k_y) = \sum_{j=0}^{m} \sum_{i=0}^{j} A_{l,i} \cos[l(k_x - k_{x0})] \cos[i(k_y - k_{y0})],$$

$$(1)$$

where $l = j - i$; $A_{l,i}$ are the adjustable parameters for different energy surfaces in a k_x-k_y plane with $\boldsymbol{k}$-point (k_{x0}, k_{y0}) at the center; and m denotes a positive integer, being no less than the natural numbers i and j, namely $m \geqslant j \geqslant i$. For a finite value of m, the number of terms in the trigonometric polynomial $E(k_x, k_y)$ should be $N_{m+1} = N_m + (m + 2)$. For $m = 1$, the first term $N_1 = 3$. In principle, the larger the value of m, the more complex the energy surface represented by the model. As m can be infinite, the function $E(k_x, k_y)$ can be considered as a series related to m.

For $(k_{x0}, k_{y0}) = (0, 0)$, four types of hatlike bands (see Fig. 1) can be derived from the dispersion model Eq. (1) with different m and $A_{l,i}$. These bands include the safety, Mexican, wavy brim, and wavy brim bucket hats. Detailed descriptions of these hats and the associated coefficients $A_{l,i}$ were presented in Sec. I of the Supplemental Material [45].

Based on the obtained hat bands, the corresponding DOS can be calculated as

$$g(E) = \frac{1}{(2\pi)^2} \int \frac{1}{|\nabla_{\boldsymbol{k}} E|} \, dl_E. \qquad (2)$$

The derivation of this equation is presented in Sec. II of the Supplemental Material [45]. From $E(k_x, k_y)$, the DOSs of the different hats were evaluated using discrete numerical calculations (right side of the corresponding 3D band in Fig. 1). As marked in the pictures, these hat bands generate two types of VHSs: (i) VHS-I, a Heaviside step function discontinuity [41] at maximum $E = E_{\max}$, and (ii) VHS-II, a divergence in the DOS due to the appearance of saddle points with $|\nabla_{\boldsymbol{k}} E| \to 0$. Specifically, the safety hat has only VHS-I, whereas the wavy brim bucket hat holds only VHS-II. Mexican and wavy brim hats exhibit both VHS-I and VHS-II. As VHS-II is a strongly localized state, materials with VHS-II are usually considered ideal for realizing interesting and strongly correlated physics [46–48].

According to the above results, the wavy brim bucket hat is more intriguing than the other hats due to the coexistent flat-band state and brim valleys. To further explore the possible physics and practical applications, the matrix materials of the wavy brim bucket hat should be investigated in the future. As spontaneous valley polarizations [8] can be induced by breaking both time reversal and spatial inversion symmetries, we focused on the single-spin wavy brim bucket hat band in
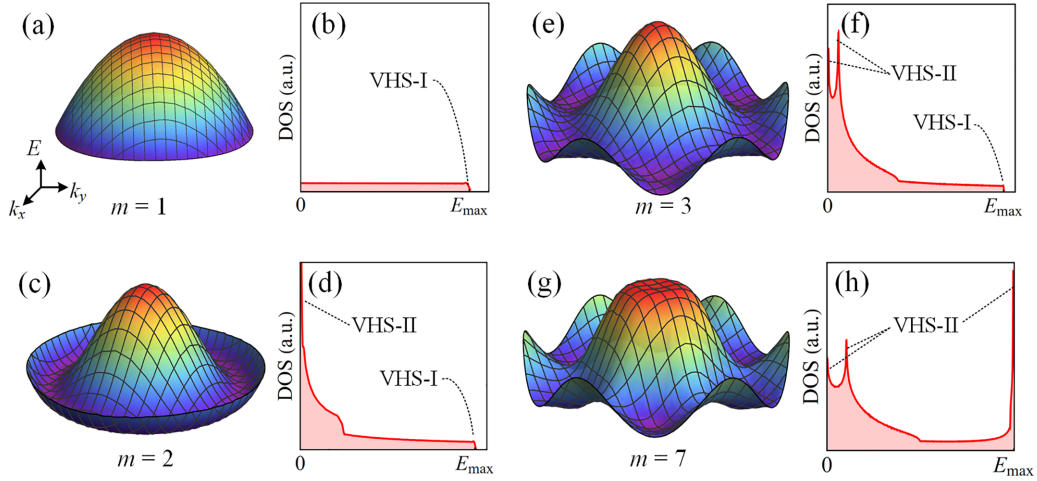
FIG. 1. Four types of hatlike bands together with the corresponding DOS: (a), (b) safety hat; (c), (d) Mexican hat; (e), (f) wavy brim hat; and (g), (h) wavy brim bucket hat. All the 3D $E(k_x, k_y)$ bands are plotted within a circular area defined by $k_x^2 + k_y^2 \leqslant 0.25$, aiming to simulate the scenario of a real hat.

a new 2D FM material, namely Janus GdIH ML. Before investigating the single-spin wavy brim bucket hat, the structure and basic properties of the GdIH ML were examined.

B. Structure, stability, and magnetic state of Janus GdIH ML

The synthesized bulk GdI_2 [49–51] has a 2H-MoS_2-type vdW layered structure, and its ML has a smaller exfoliation energy ($0.24 \, \text{J/m}^2$ [31]) with respect to that of graphene ($0.37 \, \text{J/m}^2$ [52]). Thus, many efforts have been devoted to the family of GdX_2 ($X = $ F, Cl, Br, and I) MLs, focusing on their magnetic and electronic properties [31,53,54]. In this work, we focused only on the Janus GdIH ML because (i) it has a particular wavy brim bucket hat band edge, whereas other GdX_2 MLs have a wavy brim hat band edge [31,54]; (ii) in the experiment, a similar Janus-structured MoSH ML was synthesized by substituting the top-layer S atoms of 2H-MoS_2 with H atoms using gentle H_2 plasma treatment [55].

(1) *Structure*. Similar to the MoSH ML [55,56], the optimized GdIH ML adopts a closely packed sandwich structure [Figs. 2(a) and 2(b)] and holds trigonal space group symmetry ($P3m1$, no. 156) with inversion asymmetry. Each intermediate Gd atom was bonded to three top-layer I atoms and three underlying H atoms, forming a trigonal prism coordination environment with C_{3v} point-group symmetry. The lattice constants of GdIH ML were fully relaxed to $a = b = 3.807$ Å and smaller than that (4.099 Å [31]) of GdI_2 ML due to the hydrogenation effect. As shown in Fig. 2(b), the bond length (3.09 Å) of Gd-I was significantly longer than that (2.38 Å) of Gd-H. According to the electron localization function (ELF) [57] [Figs. 2(c) and 2(d)] of the GdIH ML, the bonds of both Gd-I and Gd-H exhibited ionic features. Additionally, the center of a triangle Gd cluster, i.e., the interstitial area of the hexagonal lattice, contained a strongly localized electron (referred to as "anionic" electron e^-) [Figs. 2(c) and 2(d)]. This indicates that GdIH ML is a typical 2D electride material, that is, an electrene [58]. Considering the valence state of all atoms, the chemical formula of GdIH ML can be expressed

as $Gd^{3+}I^-H^- \cdot e^-$, like the ideal ferrovalley semiconductor LaH_2 ML [59].

(2) *Stability*. To examine the stability of GdIH ML, we first evaluated its formation energy defined as $E_f = (\mu_{\text{Gd}} + \mu_{\text{H}} + \mu_{\text{I}} - E_{\text{GdIH}})/3$, where μ_{Gd}, μ_{H}, and μ_{I} are the chemical potentials of Gd, H, and I atoms in their ground states, respectively. $E_f = 1.33$ eV per atom was obtained. This indicated
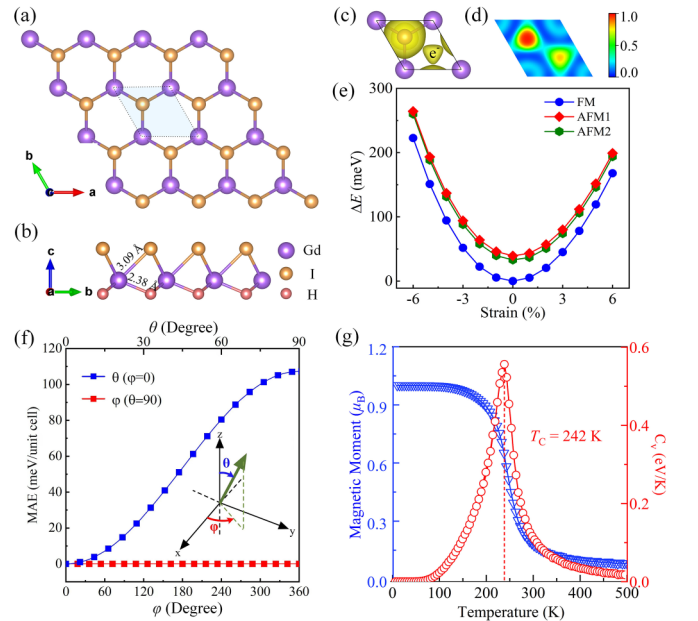

FIG. 2. (a) Top and (b) side views of the optimized structure of GdIH ML. Its primitive cell is marked by the shaded area. (c) ELF in real space and (d) its 2D map projected onto the xy plane. (e) Relative total energies of different magnetic states (FM, AFM1, and AFM2) as functions of external strains in the range from -6% to 6%. (f) MAE in various magnetization directions on the yz plane (indicated by blue points) and the xy plane (indicated by red points). (g) The magnetic moment and heat capacity (C_V) as functions of temperature in the Monte Carlo simulation.

the formation of GdIH ML to be an exothermic process. As it is larger than that [1.23 eV, $E_f' = (\mu_{Gd} + 2\mu_I - E_{GdI_2})/3$] of GdI$_2$ ML, the H$_2$ plasma treatment as in MoSH ML [55] should be feasible for producing Janus GdIH ML. Then, we calculated the phonon spectrum of the GdIH ML. As no imaginary frequencies were observed (Fig. S2 of Sec. III in the Supplemental Material [45]), the GdIH ML was considered dynamically stable. The elastic constants were calculated as C$_{11}$ = 242.31 N/m, C$_{22}$ = 236.4 N/m, C$_{12}$ = 66.38 N/m, and C$_{44}$ = 82.17 N/m, which well satisfied the Born-Huang criteria [60], including C$_{11} > 0$, C$_{11}$C$_{22} >$ C$_{12}^2$, and C$_{44} > 0$. Therefore, the GdIH ML was also considered mechanically stable. For a 2D material, the gravity-induced bending h/l can be estimated as [61] $h/l \approx (\sigma g l / E_{2D})^{1/3}$, where h is the out-of-plane deformation, $\sigma = 3.77 \times 10^{-6}$ kg/m^2 represents the surface density, l represents the size ($\sim$100 μm) of possible free-standing flake, g represents the gravitational acceleration, and E_{2D} is Young's modulus. For $\sigma = 3.77 \times 10^{-6}$ kg/m^2 and $E_{2D} = ($C$_{11}^2 - C_{12}^2)/C_{11} = 224.13$ GPa nm, the h/l of GdIH ML was evaluated to be 2.56×10^{-4}, which was of the same order of magnitude as that of graphene [61] and MnPSe$_3$ [62] ML. This indicates that the stiffness of GdIH ML was sufficient to withstand its own weight, similar to graphene and MnPSe$_3$ ML.

(3) *Magnetic ground state and its stability*. To determine the low-energy magnetic state of the GdIH ML, we constructed a redefined (2**a**, **a**+2**b**) supercell and considered possible magnetic configurations, including paramagnetic (PM), collinear ferromagnetic (FM), and different collinear antiferromagnetic (AFM) states (Fig. S3 of Sec. IV in the Supplemental Material [45]). Spin polarization was considered for the FM and AFM states, but not for the PM state. According to the calculated energies of these magnetic configurations, the FM state was the most stable, even under different mechanical strains [Fig. 2(e)], usually induced by the support substrate due to the existence of an inevitable lattice mismatch [63,64]. The optimized magnetic moment of FM GdIH ML is 1 μ$_B$ per unit cell. Due to the features of electrenes, interstitial anionic electrons mainly contribute to the magnetic moment (Fig. S3 of Sec. IV in the Supplemental Material [45]). In our calculations, the valence electron configurations of the H, I, and Gd atoms were $1s^1$, $5s^25p^5$, and $5p^66s^25d^1$. According to our Bader charge analysis, [65] each H and I atom snatched one electron from the 6s state of the Gd atom, forming a stable closed-shell structure with antiparallel spin, i.e., $1s^2$ ($\downarrow\uparrow$) and $5p^6$ ($\downarrow\uparrow\downarrow\uparrow\downarrow\uparrow$), respectively. Then, the remaining $5d^1$ of the Gd atom left its atomic central and formed an unpaired local anionic electron e^- in the interstitial area due to the d-d hybridization among Gd atoms, giving rise to a magnetic moment of 1 μ$_B$.

Notably, magnetocrystalline anisotropy (MCA) plays a critical role in stabilizing long-range FM ordering in 2D material [66,67]. Thus, examining the magnetic anisotropy energy (MAE) of GdIH ML, which often determines the capacity of FM ordering to resist heat fluctuations, is necessary; the larger the MAE, the better the thermal stability of the long-range FM ordering. The relative energies along different magnetizing directions were obtained by considering the spin-orbital coupling (SOC) effect. As shown in Fig. 2(f): (i) the easy axis of GdIH ML was along the out-of-plane (001) z direction, like

the synthesized CrI$_3$ ML [67]; (ii) the magnetization in the x-y plane was isotropic, indicating that GdIH ML belongs to *XY* ferromagnet [66]; (iii) the obtained MAE, the relative energy of the hard axis (100) or (010) with respect to the easy axis (001), was up to 107 μeV, significantly larger than the experimentally reported values of the Fe ML/Rh(111) (80 μeV) [68]. Given that the GdIH ML has a hexagonal lattice, there may exist frustrated magnetic states, as suggested in previous studies [69–71]. To investigate this possibility, we constructed a (3×3×1) supercell and designed potential frustrated non-collinear AFM configurations (see Fig. S4 in Sec. IV of the Supplemental Material [45]). Further calculations of relative energies (Table S2 in Sec. IV of the Supplemental Material [45]) revealed that all the considered frustrated states are unstable with respect to the out-of-plane FM ground state. This means that the frustrated magnetic states do not exist under intrinsic conditions, in alignment with the out-of-plane easy axis and significant MAE of the GdIH ML.

To further explore the thermal stability of the FM ground state, we evaluated the Curie temperature (T_C) using different methods, including the mean-field approximation (MFA), Monte Carlo (MC) simulations, and first-principles molecular-dynamics simulations. Based on the possible magnetic states (Fig. S3 of Sec. IV in the Supplemental Material [45]), the first- (J_1) and second- (J_2) nearest-neighbor magnetic exchange interactions were evaluated using the classical Heisenberg model, $H = -\sum_{i,j} J_1 S_i S_j - \sum_{k,l} J_2 S_k S_l$. With information on the coordination patterns of the local magnetic moments, the derived expressions of J_1 and J_2 are $J_1 = -(E_{AFM2} - 2E_{AFM1} + E_{FM})/8m^2$ and $J_2 = -(E_{AFM1} - E_{AFM2})/4m^2$, where E_{FM}, E_{AFM1}, and E_{AFM2} are the total energies of FM, AFM1, and AFM2, respectively, and m denotes the local magnetic moment. For GdIH ML, the J_1 and J_2 were estimated to be 5.72 and 1.6 meV, respectively. Based on the obtained J_1 and J_2 values, T_C was calculated as 286 K using MFA (Sec. V in the Supplemental Material [45]). As the MFA method cannot accurately describe the magnetic percolation effect [72], it usually overestimates T_C. Thus, we performed a numerical MC simulation using the Wolff algorithm [73] in a constructed 16×16 supercell. As illustrated in Fig. 2(g), the temperature-dependent magnetic moment per unit cell and specific heat (C_V) obtained from the MC simulations revealed that the T_C of the GdIH ML was approximately 240 K, This was consistent with the MFA results and our first-principles molecular simulation [Fig. S2(b) of Sec. III in the Supplemental Material [45]]. Compared with experimentally reported systems, such as CrI$_3$ (45 K [67]), CrBr$_3$ (34 K [74]), PTC-Fe (15 K [75]), and Fe-T4PT (1.8 K [76]), the proposed GdIH ML is a more promising 2D magnet for spintronic applications at higher temperatures.

C. Wavy brim bucket hat band in valence-band edge of GdIH ML

Figure 3(a) presents the color map of the spin-polarized electronic band structure of the GdIH ML considering the SOC with the projection of the spin operator $\hat{s}_z$. As shown, GdIH ML featured as a bipolar magnetic semiconductor [18] with an indirect band gap of 0.41 eV, in which the valence-band edge (VBE) and conduction-band edge (CBE) were fully
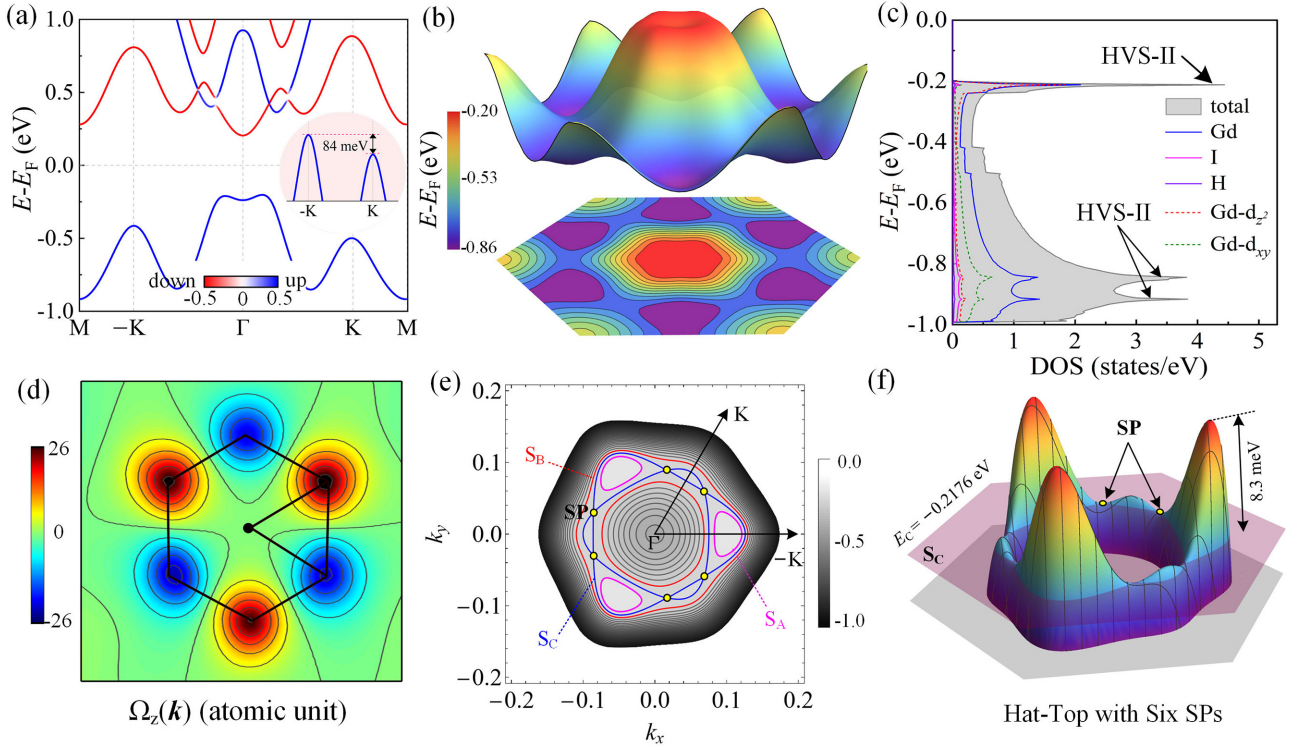
FIG. 3. (a) The color map of the band structure for GdIH ML with the projection of spin operator $\hat{s}_z$ considering SOC. (b) The 3D surface $E(k_x, k_y)$ for the valence-band edge in the whole 2D first Brillouin zone. Below is the corresponding 2D contour map. (c) DOS, and atomic and orbital projected DOS in the energy window of $[-1, 0]$ eV. (d) The contour plot of Berry curvatures in the BZ. (e) The energy contours of the fitted Eq. (1) on the k_x-k_y plane for the top of the wavy brim bucket hat. (f) The zoomed-in view of the lens for the 3D hat-top with six SPs.

spin-polarized with opposite spin directions. This is highly conducive to the tunability of spin polarization by applying the accessible gate voltage, giving rise to the electrical controlling of magnetism [18]. The spin-up valence-band edge exhibited the typical features of the proposed wavy brim bucket hat: (i) a complete wavy brim bucket hat band appeared in the whole first Brillouin zone, as is shown in Fig. 3(b); (ii) the 3D bands were fitted well using the dispersion model [Eq. (1)] with $m = 7$ (Fig. S5 and Table S3 in Sec. VI of the Supplemental Material [45]); (iii) three VHS-II [Fig. 3(c)] were formed in the corresponding DOS like that in the model case [Fig. 1(h)]. These results were confirmed using the more accurate HSE06 method [bands in Fig. S6(a) of Sec. VII in the Supplemental Material [45]]. Additionally, we have presented some more interesting details about the wavy brim bucket hat related to single-spin characteristics in the following subsections.

(1) *Spontaneous valley polarization and high carrier mobility in the hexagonal wavy brim.* Along the wavy brim of the wavy brim bucket hat, we identified the existence of an energy difference [84 meV, see Fig. 3(a)] between the peaks of the wavy brim at $-K$ and K. This indicated the emergence of spontaneous valley polarization. In an inversion asymmetrical FM system, two types of spin splitting, i.e., Δ_{mag} and Δ_{SOC}, can usually be induced by the magnetic exchange interaction and SOC effect, respectively [77]. For GdIH ML, when the SOC is switched off, the values of Δ_{mag} at $-K$ and K should be equal [Fig. S6(b) of Sec. VII in the Supplemental Material [45]], i.e., $\Delta_{\text{mag}}(-K) = \Delta_{\text{mag}}(K)$. However, if the

SOC is turned on, the values of Δ_{SOC} at $-K$ and K exhibit opposite signs, i.e., $-\Delta_{\text{SOC}}(-K) = \Delta_{\text{SOC}}(K)$, due to the breaking of inversion symmetry. Therefore, considering SOC, the spin splitting at $-K$ and K should be $\Delta_{\text{mag}} + \Delta_{\text{SOC}}$ and $\Delta_{\text{mag}} - \Delta_{\text{SOC}}$, respectively. Consequently, the valley degeneracy between $-K$ and K is eliminated, giving rise to intrinsic ferrovalley ordering for valley, like the FM state for spin.

To examine the possible applications of the spontaneous valley polarization in a wavy brim bucket hat brim, we computed the Berry curvature $\boldsymbol{\Omega}_z(\boldsymbol{k})$ [Fig. 3(d)] using the Kubo method [78] (Sec. VIII in the Supplemental Material [45]), which is a key parameter for understanding the electronic transport properties. According to the results, the $\boldsymbol{\Omega}_z(\boldsymbol{k})$ of GdIH ML exhibited peaks at both $-K$ and K valleys but with opposite sign due to the breaking of inversion symmetry. Thus, an intriguing anomalous valley Hall effect [8] was induced (Fig. S7 of Sec. IX in the Supplemental Material [45]) after the application of an external in-plane electric field. In the valley Hall effect, an additional charge Hall current appeared due to spontaneous valley polarization.

As the transport properties of carriers are mainly governed by their mobilities, we theoretically predicted the carrier mobilities of brim $-K$ valleys in GdIH ML. Within the framework of the deformation potential theory [79,80], the carrier mobilities of 2D materials can be estimated as $\mu_{\text{2D}} = e\hbar^3 C_{\text{2D}}/k_B T m_e^* m_d E_l^2$. The three key factors are as follows: the effective mass m^*, deformation potential E_l, and elastic modulus C_{2D}. According to the results (Table S4 and Figs. S8 − S10 of Sec. X in the Supplemental Material [45]),

the mobilities of brim holes around $-K$ were calculated as $2.7 \times 10^4 \, \text{cm}^2 \, \text{V}^{-1} \text{s}^{-1}$ ($2.9 \times 10^4 \, \text{cm}^2 \, \text{V}^{-1} \text{s}^{-1}$) along $y(x)$ directions. As a relatively small effective mass stemmed from the massive Dirac dispersion, the carrier mobilities were higher than that of MoS_2 ML ($0.2 \times 10^3 \, \text{cm}^2 \, \text{V}^{-1} \text{s}^{-1}$ [81]), and comparable to that of the prominent black phosphorus ML [$(1.0 - 2.6) \times 10^4 \, \text{cm}^2 \, \text{V}^{-1} \text{s}^{-1}$ along the y direction [82]]. In this regard, obtaining the desirable "high-speed and valley-related" carrier transport in the future nanodevices would be possible based on the hole-doped GdIH ML.

(2) *Single spin van Hove singularity in the flat top.* Around the center of the BZ, the wavy brim bucket hat top is almost flat, with an almost negligible band dispersion in a very narrow energy window ($\sim$10 meV), considerably smaller than the energy criterion (25–150 meV) for flat-band materials [4]. In such a window, many-body effects dominate the kinetic energy, which may give rise to correlated insulator states, non-Fermi-liquid behavior, and strong-coupling superconductivity [83]. When the Fermi level on the flat top in the vicinity of VBM was modulated by applying a gate voltage, the Fermi surfaces underwent a Lifshitz transition [84], namely a topological geometry transformation: from three isolated half-moon-like rings (e.g., S_A at an energy of -0.2142 eV) to two large concentric rings (e.g., S_B with an energy of -0.2210 eV) [Fig. 3(e)]. During such a transition, the Fermi level crossed a critical energy of $E_C = -0.2176$ eV. On this isosurface (S_C), six rings with alternating sizes were interconnected, arranged with C_{3v} point-group symmetry.

Interestingly, six special cross points corresponded to three pairs of saddle points (SPs) [Figs. 3(e) and 3(f)] located on the two sides of the $\Gamma \to K$ or $\Gamma \to -K$ paths. Around those, the gradient of eigenvalues $E(k_x, k_y)$ along all possible $\mathbf{k}$ directions should be zero, i.e., $|\nabla_k E| = 0$, and the corresponding second-order Hessian matrix $G = (\partial^2 E / \partial k_i \partial k_j)$ with $i(j) = x, y$ should be positive-semidefinite around the six $\mathbf{k}$ points. As $g(E) \propto 1/|\nabla_k E|$ [Eq. 2], a divergence, namely VHS-II, with $g(E) \to \infty$ emerged in the DOS when $E = E_C$ [Fig. 3(c)]. Usually, VHS-II can give rise to new strongly correlated phases [46], such as superconductivity [47] and density waves [48]. In particular, VHS-II of the GdIH ML is completely spin-polarized; hence, it is promising for obtaining desirable ferromagnetic superconductors [85,86].

D. Simplified two-band Hamiltonian model for the wavy brim bucket hat band

Considering the FM order, the magnetic space group (MSG) of GdIH ML should be the "black-white" group $P3m'1$ (156.51), belonging to the type-III MSG without antitranslation symmetry. Under the corresponding symmetry operation, the localized anionic electron (from $5d^1$ of Gd atoms) with an equivalent Wyckoff position $(0, 0, z|0, 0, m_z)$ should obey the C_{3v} point group symmetry. Therefore, the d orbitals were split into three categories: $A_1(d_{z^2})$, $E(d_{xz}, d_{yz})$, and $E(d_{xy}, d_{x^2-y^2})$. According to the first-principles fat-band analysis (Fig. S11 of Sec. XI in the Supplemental Material [45]), d_{xy}, $d_{x^2-y^2}$, and d_{z^2} contributed mainly to the Bloch states of the GdIH ML near the Fermi level. Based on the symmetric matching principles based on the molecular orbital theory [87], the vertical mirror symmetries $\hat{\sigma}_v$ enable the orbital hybridization between
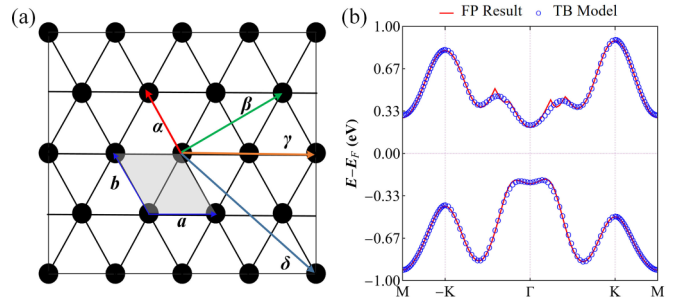

FIG. 4. (a) The model diagram includes nearest-neighbor (α), next-nearest-neighbor (β), third-nearest-neighbor (γ), and fourth-nearest-neighbor (δ) hopping. (b) The fitted TB band structure (indicated by the blue circle) of GdIH ML together with the FP band one (indicated by the red line).

the A_1 and the two E categories. Therefore, $|\varphi_1\rangle = d_{xy}$ and $|\varphi_2\rangle = d_{x^2-y^2}$ can be reasonably considered as the bases for a two-dimensional wave functional space. Then, a simplified two-band effective Hamiltonian can be constructed by considering fourth-nearest neighbor d-d hopping [[Fig. 4(a)]:

$$H^{4th}(\mathbf{k}) = \begin{pmatrix} H_{11} & H_{12} \\ H_{12}^* & H_{22} \end{pmatrix}. \quad (3)$$

Using the tight-binding (TB) method [88,89], the matrix elements of $H^{4th}(\mathbf{k})$ can be obtained from $H_{\mu\mu'}(\mathbf{k}) = \sum_R e^{i\mathbf{k}\cdot\mathbf{R}} E_{\mu\mu'}(\mathbf{R})$. Here, $\mathbf{R}$ is the lattice vector, and the hopping integral $E_{\mu\mu'}(\mathbf{R})$ can be evaluated by

$$E_{\mu\mu'}(\mathbf{R}) = \langle \varphi_\mu(\mathbf{r}) | H^{4th}(\mathbf{k}) | \varphi_{\mu'}(\mathbf{r} - \mathbf{R}) \rangle. \quad (4)$$

For simplicity, the obtained $H_{\mu\mu'}(\mathbf{k})$ are expressed as

$$H_{11} = \sum_{n,m} A_{n,m} \cos(nk_x + mk_y) + B_{n,m} \sin(nk_x + mk_y), \quad (5)$$

$$H_{22} = \sum_{n,m} C_{n,m} \cos(nk_x + mk_y) + D_{n,m} \sin(nk_x + mk_y), \quad (6)$$

$$H_{12} = \sum_{n,m} E_{n,m} \cos(nk_x + mk_y) + F_{n,m} \sin(nk_x + mk_y), \quad (7)$$

where the coefficients $A_{n,m}$, $B_{n,m}$, $C_{n,m}$, $D_{n,m}$, $E_{n,m}$, and $F_{n,m}$ are polynomial of different hopping parameters, including ε_j, α_j, β_j, γ_j, and δ_j, which, respectively, represent the on-site energies, nearest-neighbor, next-nearest, third-nearest, and fourth-nearest neighbor hopping parameters (Table S5 of Sec. XII in the Supplemental Material [45]). Based on the TB model, we solved the eigenvalue function $E(\mathbf{k})$. Although the list of parameters was relatively complex, they fitted well using the Newton method [90]. The fitted 26 parameters for $E(\mathbf{k})$ and $H^{4th}(\mathbf{k})$ are listed in Table S6 of Sec. XIII in the Supplemental Material [45]. The corresponding two-edged TB bands are shown in Fig. 4(b). As shown, the two TB bands agreed well with the corresponding first-principles results. Therefore, the proposed wavy brim bucket hat can be described well by the effective Hamiltonian model [Eq. (3)], which will be useful in future studies on the transport properties, optical properties, and many-body physics of the wavy brim bucket hat edge band.
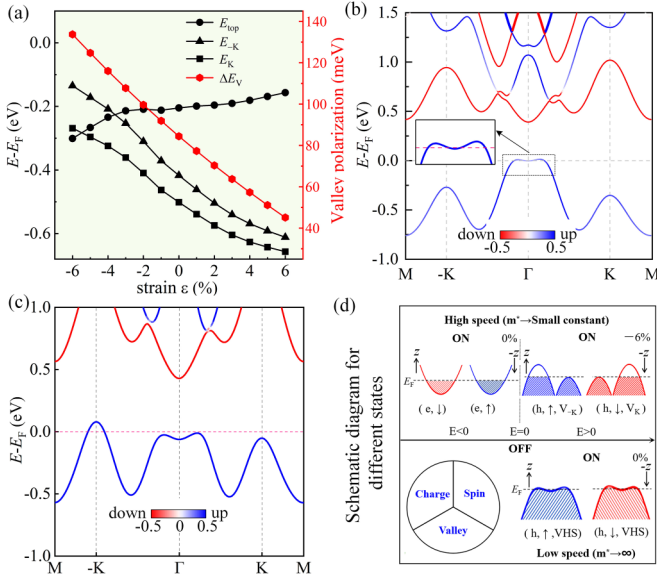
FIG. 5. (a) The energies for the maximum of the wavy brim bucket hat top (E_{top}), K valley (E_K), −K ($E_{−K}$) valley, and the values of valley polarization (ΔE_V) as functions of external strains ranging from −6% to 6%. The color map of the band structures with the projection of spin operator $\hat{s}_z$ considering the SOC at different carrier doping concentrations for (b) unstrained and GdIH ML with 0.06 electrons per primitive cell (4.78×10^{13} cm^{-2}) and (c) −6%-strained GdIH ML with 0.06 holes per primitive cell (5.41×10^{13} cm^{-2}). (d) Schematic diagram illustrating different states.

E. Adjustability of different electronic states in GdIH ML

For practical device applications, the switchability and adjustability of the electronic states of new 2D materials are highly desirable. The electronic properties can be experimentally engineered using following two methods: (i) mechanical strains, which can be induced by stretching or bending of a flexible substrate [91], and (ii) electrolyte gate, which can generate high doping level of electron or hole carriers up to 10^{15} cm^{-2} in 2D materials [92,93]. To explore the impact of external strain on the wavy brim bucket hat of GdIH ML, we first recalculated the band structures (Fig. S12 of Sec. XIV in the Supplemental Material [45]) under different strains ranging from −6% to 6%, which are accessible in experiments. As shown in Fig. 5(a), the valley polarizations (ΔE_V) between −K and K valleys in the brim almost changed linearly with respect to the applied strains, satisfying the expression $\Delta E_V = -7.58\varepsilon + 84$ (meV). This stems from the similar changing trend of energies at −K ($E_{−K}$) and K (E_K) valleys. When the compressive strain was larger than 4%, the maximum of the hat-top in the $\Gamma \to K$ path was smaller than $E_{−K}$, and smaller than E_K under −6% strain. This implies that the proposed wavy brim bucket hat undergoes noticeable distortion with the hat top sinking and hat brim rising. Consequently, the formed clean energy window (∼135 meV) occupies only the −K valley band, which provides the possibility to obtain the fully valley polarized high-speed holes.

Combined with mechanical strains, we further examined the possible conductive ON states by applying carrier doping.

For unstrained GdIH ML, the flat-top can be well preserved with a modest hole doping (∼10^{13} cm^{-2}), and the Fermi level can be precisely shifted in the hat-top energy window [∼10 meV, see Fig. 5(b)]. If the dispersion is ignored, m^* approaches infinity, and the corresponding mobility of heavy fermions is zero, that is, ultralow speed. Moreover, the narrow conductive window provides the opportunity to get the Lifshitz transition and single-spin metallic VHS-II state (h, ↑, VHS) as discussed above.

Under the strain of −6%, hole doping can move the Fermi level emerging into the −K valley, forming a single-spin and -valley metallic state (h, ↑, V$_{−K}$) [Fig. 5(c)]. From the point of view of carrier mobilities, the hats related to (h, ↑, VHS) and (h, ↑, V$_{−K}$) are two extreme opposite states, which can be viewed as a "bipolar" (ultra-low-speed vs ultra-high-speed), corresponding to heavy and massive Dirac fermions, respectively. Furthermore, apart from the states on the hat band, another high-speed conductive ON state (e, ↓) existed with a large intrinsic carrier mobility of 1.8×10^4 cm^2 V^{-1}s^{-1} along the y direction (Table S4 of Sec. X in the Supplemental Material [45]). This can be induced by electron doping (Fig. S13 of Sec. XV in the Supplemental Material [45]). Contrary to (h, ↑, V$_{−K}$), such a state has opposite spin direction due to the bipolar magnetic feature (↑ vs ↓). In this regard, GdIH ML can be viewed as a rare *double bipolar* semiconductor that is promising for future multifunctional nanodevices. Figure 5(d) shows a schematic of the transition between the three states by strain and carrier doping. Notably, if the magnetization direction is tuned to −z axis by an external magnetic field, both the spin and valley of the three identified states will be reversed, changing to (h, ↓, VHS), (h, ↓, V$_{−K}$), and (e, ↑).

IV. CONCLUSIONS

In summary, by proposing a general band dispersion model for different hatlike bands, we identified a single-spin wavy brim bucket hat band exhibiting a flat top and a wavy brim with six valleys. Using first-principles calculations, we demonstrated that a new Janus FM electrene 2D material, GdIH ML, can harbor such a special hat state. The results can be summarized in the following points: (i) it is an *XY* magnet with a large MAE and robust FM ground state near ambient temperature; (ii) due to magnetic exchange interaction, its wavy brim bucket hat is fully spin-polarized, resulting in single-spin VHS-II on the top and sizable spontaneous valley polarization along the brim; (iii) based on group theory analysis, a simplified two-band effective Hamiltonian is constructed, which can well describe the whole wavy brim bucket hat band; (iv) applying strains and carrier doping, different conductive ON states, including (h, ↑, VHS), (h, ↑, V$_{−K}$), (e, ↓), (h, ↓, VHS), (h, ↓, V$_{−K}$), and (e, ↑) can be obtained, which is promising for multifunctional nanodevice applications; and (v) remarkably, the special wavy brim bucket hat makes GdIH ML a rare double bipolar semiconductor.

The vdW layered bulks GdIH$_x$ ($0.67 < x < 1.0$) were first synthesized in the 1980s [94–96]. In the layered GdIH solid, monolayer Gd$_2$I$_2$H$_2$ has a completely different structure (with bilayer Gd atoms sandwiched between iodine atoms [96]) from that of our proposed Janus GdIH ML, despite

the same stoichiometry. In this regard, obtaining Janus GdIH ML directly through the conventional mechanical exfoliation approach is unlikely [94]. However, Janus GdIH ML can be synthesized using a two-step method: (i) obtaining the GdI_2 ML by mechanically exfoliating from the synthesized layered bulk GdI_2 [49–51], which has a smaller exfoliation energy ($0.24 \, \text{J/m}^2$) [31] than graphite ($0.37 \, \text{J/m}^2$ [52]) and MoS_2 ($0.27 \, \text{J/m}^2$ [97]); (ii) replacing one layer of the I atoms with hydrogen atoms by the H plasma stripping technique, which has been successfully applied in the fabrication of Janus MoSH ML [55]. To this end, our work may stimulate further experimental research on GdIH ML and wavy brim bucket hat bands.

[1] C. Kittel and P. McEuen, *Introduction to Solid State Physics* (Wiley, Hoboken, 2018)

[2] J. Singleton, *Band Theory and Electronic Properties of Solids* (Oxford University Press, Oxford, 2001), Vol. 2.

[3] A. Bansil, H. Lin, and T. Das, Colloquium: Topological band theory, Rev. Mod. Phys. **88**, 021004 (2016).

[4] N. Regnault, Y. Xu, M. R. Li, D. S. Ma, M. Jovanovic, A. Yazdani, S. Parkin, C. Felser, L. M. Schoop, and N. P. Ong, Catalogue of flat-band stoichiometric materials, Nature (London) **603**, 824 (2022).

[5] N. P. Armitage, E. J. Mele, and A. Vishwanath, Weyl and Dirac semimetals in three-dimensional solids, Rev. Mod. Phys. **90**, 015001 (2018).

[6] J. Xiao and B. Yan, First-principles calculations for topological quantum materials, Nat. Rev. Phys. **3**, 283 (2021).

[7] R. A. de Groot, F. M. Mueller, P. G. van Engen, and K. H. J. Buschow, New class of materials: Half-metallic ferromagnets, Phys. Rev. Lett. **50**, 2024 (1983).

[8] W. Y. Tong, S. J. Gong, X. Wan, and C. G. Duan, Concepts of ferrovalley material and anomalous valley Hall effect, Nat. Commun. **7**, 13612 (2016).

[9] B. Razavi, *Fundamentals of Microelectronics* (Wiley, Hoboken, 2021).

[10] I. Žutić, J. Fabian, and S. D. Sarma, Spintronics: Fundamentals and applications, Rev. Mod. Phys. **76**, 323 (2004).

[11] J. R. Schaibley, H. Yu, G. Clark, P. Rivera, J. S. Ross, K. L. Seyler, W. Yao, and X. Xu, Valleytronics in 2D materials, Nat. Rev. Mater. **1**, 16055 (2016).

[12] M. Z. Hasan and C. L. Kane, Colloquium: Topological insulators, Rev. Mod. Phys. **82**, 3045 (2010).

[13] Z. Li, J. Zhuang, L. Wang, H. Feng, Q. Gao, X. Xu, W. Hao, X. Wang, C. Zhang, and K. Wu, Realization of flat band with possible nontrivial topology in electronic Kagome lattice, Sci. Adv. **4**, eaau4511 (2018).

[14] Y. Cao, V. Fatemi, S. Fang, K. Watanabe, T. Taniguchi, E. Kaxiras, and P. Jarillo Herrero, Unconventional superconductivity in magic-angle graphene superlattices, Nature (London) **556**, 43 (2018).

[15] H. Ishizuka and Y. Motome, Dirac half-metal in a triangular ferrimagnet, Phys. Rev. Lett. **109**, 237207 (2012).

[16] X. L. Wang, Proposal for a new class of materials: Spin gapless semiconductors, Phys. Rev. Lett. **100**, 156404 (2008).

[17] M. Jugovac, I. Cojocariu, J. Sánchez Barriga, P. Gargiani, M. Valvidares, V. Feyer, S. Blügel, G. Bihlmayer, and P. Perna, Inducing single spin-polarized flat bands in monolayer graphene, Adv. Mater. **35**, 2301441 (2023).

[18] X. Li, X. Wu, Z. Li, J. Yang, and J. Hou, Bipolar magnetic semiconductors: A new class of spintronics materials, Nanoscale **4**, 5680 (2012).

[19] D. Xiao, W. Yao, and Q. Niu, Valley-contrasting physics in graphene: Magnetic moment and topological transport, Phys. Rev. Lett. **99**, 236809 (2007).

[20] K. F. Mak, K. He, J. Shan, and T. F. Heinz, Control of valley polarization in monolayer MoS_2 by optical helicity, Nat. Nanotechnol. **7**, 494 (2012).

[21] Y. Li, J. Ludwig, T. Low, A. Chernikov, X. Cui, G. Arefe, Y. D. Kim, A. M. van der Zande, A. Rigosi, H. M. Hill, S. H. Kim, J. Hone, Z. Li, D. Smirnov, and T. F. Heinz, Valley splitting and polarization by the zeeman effect in monolayer $MoSe_2$, Phys. Rev. Lett. **113**, 266804 (2014).

[22] C. Zhao, T. Norden, P. Zhang, P. Zhao, Y. Cheng, F. Sun, J. P. Parry, P. Taheri, J. Wang, and Y. Yang, Enhanced valley splitting in monolayer WSe_2 due to magnetic exchange field, Nat. Nanotechnol. **12**, 757 (2017).

[23] D. MacNeill, C. Heikes, K. F. Mak, Z. Anderson, A. Kormányos, V. Zólyomi, J. Park, and D. C. Ralph, Breaking of valley degeneracy by magnetic field in monolayer $MoSe_2$, Phys. Rev. Lett. **114**, 037401 (2015).

[24] Y. Ye, J. Xiao, H. Wang, Z. Ye, H. Zhu, M. Zhao, Y. Wang, J. Zhao, X. Yin, and X. Zhang, Electrical generation and control of the valley carriers in a monolayer transition metal dichalcogenide, Nat. Nanotechnol. **11**, 598 (2016).

[25] S. A. Vitale, D. Nezich, J. O. Varghese, P. Kim, N. Gedik, P. Jarillo-Herrero, D. Xiao, M. Rothschild, X. Yin, and X. Zhang, Valleytronics: Opportunities, challenges, and paths forward, Small **14**, 1801483 (2018).

[26] H. Hu, W. Y. Tong, Y. H. Shen, X. Wan, and C. G. Duan, Concepts of the half-valley-metal and quantum anomalous valley Hall effect, npj Comput. Mater. **6**, 129 (2020).

[27] X. Zhou, R. W. Zhang, Z. Zhang, W. Feng, Y. Mokrousov, and Y. Y, Sign-reversible valley-dependent Berry phase effects in 2D valley-half-semiconductors, npj Comput. Mater. **7**, 160 (2021).

[28] G. Kresse and J. Furthmüller, Efficient iterative schemes for ab initio total-energy calculations using a plane-wave basis set, Phys. Rev. B **54**, 11169 (1996).

[29] J. P. Perdew, K. Burke, and M. Ernzerhof, Generalized gradient approximation made simple, Phys. Rev. Lett. **77**, 3865 (1996).

[30] S. Grimme, J. Antony, S. Ehrlich, and H. Krieg, A consistent and accurate ab initio parametrization of density functional dispersion correction (DFT-D) for the 94 elements H-Pu, J. Chem. Phys. **132**, 154104 (2010).

[31] H. X. Cheng, J. Zhou, W. Ji, Y. N. Zhang, and Y. P. Feng, Two-dimensional intrinsic ferrovalley GdI_2 with large valley polarization, Phys. Rev. B **103**, 125121 (2021).

[32] J. Heyd, G. E. Scuseria, and M. Ernzerhof, Hybrid functionals based on a screened Coulomb potential, J. Chem. Phys. **118**, 8207 (2003).

[33] S. W. Kim, H. J. Kim, S. Cheon, and T. H. Kim, Circular dichroism of emergent chiral stacking orders in quasi-one-dimensional charge density waves, Phys. Rev. Lett. **128**, 046401 (2022).

[34] T. Fukui, Y. Hatsugai, and H. Suzuki, Chern numbers in discretized Brillouin zone: Efficient method of computing (spin) hall conductances, J. Phys. Soc. Jpn. **74**, 1674 (2005).

[35] F. Guinea, A. H. Castro Neto, and N. M. R. Peres, Electronic states and Landau levels in graphene stacks, Phys. Rev. B **73**, 245426 (2006).

[36] T. Stauber, N. M. R. Peres, F. Guinea, and A. H. Castro Neto, Fermi liquid theory of a Fermi ring, Phys. Rev. B **75**, 115425 (2007).

[37] E. V. Castro, K. S. Novoselov, S. V. Morozov, N. M. R. Peres, J. M. B. Lopes dos Santos, J. Nilsson, F. Guinea, A. K. Geim, and A. H. Castro Neto, Biased bilayer graphene: Semiconductor with a gap tunable by the electric field effect, Phys. Rev. Lett. **99**, 216802 (2007).

[38] V. Zólyomi, N. D. Drummond, and V. I. Fal'ko, Band structure and optical transitions in atomic layers of hexagonal gallium chalcogenides, Phys. Rev. B **87**, 195403 (2013).

[39] N. Jia, Y. Shi, Z. Lv, J. Qin, J. Cai, X. Jiang, J. Zhao, and Z. Liu, Tetragonal Mexican-hat dispersion and switchable half-metal state with multiple anisotropic Weyl fermions in penta-graphene, New J. Phys. **25**, 033033 (2023).

[40] M. W. Chen, H. Kim, D. Ovchinnikov, K. Agnieszka, T. Heine, O. Renault, and A. Kis, Large-grain MBE-grown GaSe on GaAs with a Mexican hat-like valence band dispersion, npj 2D Mater. Appl. **2**, 2 (2018).

[41] L. Seixas, A. S. Rodin, A. Carvalho, and A. H. Castro Neto, Multiferroic two-dimensional materials, Phys. Rev. Lett. **116**, 206803 (2016).

[42] T. Cao, Z. Li, and S. G. Louie, Tunable magnetism and half-metallicity in hole-doped monolayer GaSe, Phys. Rev. Lett. **114**, 236602 (2015).

[43] D. Wickramaratne, F. Zahid, and R. K. Lake, Electronic and thermoelectric properties of van der Waals materials with ring-shaped valence bands, J. Appl. Phys. **118**, 075101 (2015).

[44] A. Kuc, T. Cusati, E. Dib, A. F. Oliveira, A. Fortunelli, I. Giuseppe, T. Heine, and G. Fiori, High-performance 2D p-type transistors based on GaSe layers: An *ab initio* study, Adv. Electron. Mater. **3**, 1600399 (2017).

[45] See Supplemental Material at http://link.aps.org/supplemental/10.1103/PhysRevB.110.075412 for four distinct hat-like bands from Eq. (1) (Sec. I); the density of states for a 2D system (Sec. II); the dynamical and thermal stabilities of GdIH ML (Sec. III); the different magnetic states (Sec. IV); the Curie temperature calculated by the MFA method (Sec. V); the fitted wavy brim bucket hat band and parameters for GdIH ML (Sec. VI); the band structures of GdIH ML computed using different methods (Sec. VII); the method for the calculation of Berry curvature (Sec. VIII); the anomalous valley Hall effect in GdIH ML (Sec. IX); the carrier mobilities of GdIH ML (Sec. X); the orbital-resolved band structure of GdIH ML (Sec. XI); the expression of the coefficients in Eqs. (5)–(7) (Sec. XII); the fitted on-site energies and hoping parameters (Sec. XIII); the electronic band structures of GdIH ML at strains from −6% to 6% (Sec. XIV); and the band structure of −6%-strained GdIH ML with electron doping (Sec. XV). It also contains Refs. [71,82].

[46] G. Li, A. Luican, J. Lopes dos Santos, A. Castro Neto, A. Reina, K. J, and E. Andrei, Observation of Van Hove singularities in twisted graphene layers, Nat. Phys. **6**, 109 (2010).

[47] J. González, Kohn-Luttinger superconductivity in graphene, Phys. Rev. B **78**, 205431 (2008).

[48] T. M. Rice and G. K. Scott, New mechanism for a charge-density-wave instability, Phys. Rev. Lett. **35**, 120 (1975).

[49] A. Kasten, P. H. Müller, and M. Schienle, Magnetic ordering in GdI_2, Solid State Commun. **51**, 919 (1984).

[50] C. Felser, K. Ahn, R. K. Kremer, R. Seshadri, and A. Simon, Giant Negative Magnetoresistance in GdI_2: Prediction and Realization, J. Solid State Chem. **147**, 19 (1999).

[51] K. Ahn, C. Felser, R. Seshadri, R. K. Kremer, and A. Simon, Giant negative magnetoresistance in GdI_2, J. Alloys Compd. **303–304**, 252 (2000).

[52] R. Zacharia, H. Ulbricht, and T. Hertel, Interlayer cohesive energy of graphite from thermal desorption of polyaromatic hydrocarbons, Phys. Rev. B **69**, 155406 (2004).

[53] S. Li, W. Jiang, Y. Hou, F. Zheng, X. Shao, and P. Zhang, High Curie temperatures in Gd-dihalide Janus monolayers, J. Appl. Phys. **130**, 043902 (2021).

[54] K. Sheng, H. K. Yuan, and Z. Y. Wang, Monolayer gadolinium halides, GdX_2 (X= F, Cl, Br): Intrinsic ferrovalley materials with spontaneous spin and valley polarizations, Phys. Chem. Chem. Phys. **24**, 3865 (2022).

[55] A. Y. Lu, H. Zhu, J. Xiao, C. P. Chuu, Y. Han, M. H. Chiu, C. C. Cheng, C. W. Yang, K. H. Wei, and Y. Yang, Janus monolayers of transition metal dichalcogenides, Nat. Nanotechnol. **12**, 744 (2017).

[56] P. F. Liu, F. Zheng, J. Li, J. G. Si, L. Wei, J. Zhang, and B. T. Wang, Two-gap superconductivity in a Janus MoSH monolayer, Phys. Rev. B **105**, 245420 (2022).

[57] A. Savin, R. Nesper, S. Wengert, and T. F. Fässler, ELF: The electron localization function, Angew. Chem. Int. Ed. Engl. **36**, 1808 (1997).

[58] S. Zhao, Z. Li, and J. Yang, Obtaining two-dimensional electron gas in free space without resorting to electron doping: An electride based design, J. Am. Chem. Soc. **136**, 13313 (2014).

[59] Y. Shi, N. Jia, J. Cai, Z. Lyu, and Z. Liu, 2D electrene LaH_2 monolayer: An ideal ferrovalley direct semiconductor with room-temperature ferromagnetic stability, J. Phys.: Condens. Matter **34**, 475303 (2022).

[60] F. Mouhat and F. X. Coudert, Necessary and sufficient elastic stability conditions in various crystal systems, Phys. Rev. B **90**, 224104 (2014).

[61] T. J. Booth, P. Blake, R. R. Nair, D. Jiang, E. W. Hill, U. Bangert, A. Bleloch, M. Gass, K. S. Novoselov, and M. I. Katsnelson, Macroscopic graphene membranes and their extraordinary stiffness, Nano Lett. **8**, 2442 (2008).

[62] X. Li, X. Wu, and J. Yang, Half-metallicity in $MnPSe_3$ exfoliated nanosheet with carrier doping, J. Am. Chem. Soc. **136**, 11065 (2014).

[63] S. Z. Butler, S. M. Hollen, L. Cao, Y. Cui, J. A. Gupta, H. R. Gutiérrez, T. F. Heinz, S. S. Hong, J. Huang, and A. F. Ismach, Progress, challenges, and opportunities in two-dimensional materials beyond graphene, ACS Nano **7**, 2898 (2013).

[64] M. Xu, T. Liang, M. Shi, and H. Chen, Graphene-like two-dimensional materials, Chem. Rev. **113**, 3766 (2013).

[65] G. Henkelman, A. Arnaldsson, and H. Jónsson, A fast and robust algorithm for Bader decomposition of charge density, Comput. Mater. Sci. **36**, 354 (2006).

[66] X. Jiang, Q. Liu, J. Xing, N. Liu, Y. Guo, Z. Liu, and J. Zhao, Recent progress on 2D magnets: Fundamental mechanism, structural design and modification, Appl. Phys. Rev. **8**, 031305 (2021).

[67] B. Huang, G. Clark, E. Navarro Moratalla, D. R. Klein, R. Cheng, K. L. Seyler, D. Zhong, E. Schmidgall, M. A. McGuire, and D. H. Cobden, Layer-dependent ferromagnetism in a van der Waals crystal down to the monolayer limit, Nature (London) **546**, 270 (2017).

[68] A. Lehnert, S. Dennler, P. Błoński, S. Rusponi, M. Etzkorn, G. Moulas, P. Bencok, P. Gambardella, H. Brune, and J. Hafner, Magnetic anisotropy of Fe and Co ultrathin films deposited on Rh(111) and Pt(111) substrates: An experimental and first-principles investigation, Phys. Rev. B **82**, 094409 (2010).

[69] J. S. White, C. Niedermayer, G. Gasparovic, C. Broholm, J. M. S. Park, A. Y. Shapiro, L. A. Demianets, and M. Kenzelmann, Multiferroicity in the generic easy-plane triangular lattice antiferromagnet $RbFe(MoO_4)_2$, Phys. Rev. B **88**, 060409(R) (2013).

[70] X. Feng, Z. Zhang, W. Wu, X. L. Sheng, and S. A. Yang, Quadratic nodal point in a two-dimensional noncollinear antiferromagnet, Phys. Rev. B **109**, 045423 (2024).

[71] S. Nakatsuji, N. Kiyohara, and T. Higo, Large anomalous Hall effect in a non-collinear antiferromagnet at room temperature, Nature (London) **527**, 212 (2015).

[72] K. Sato, L. Bergqvist, J. Kudrnovský, P. H. Dederichs, O. Eriksson, I. Turek, B. Sanyal, G. Bouzerar, H. Katayama-Yoshida, V. A. Dinh, T. Fukushima, H. Kizaki, and R. Zeller, First-principles theory of dilute magnetic semiconductors, Rev. Mod. Phys. **82**, 1633 (2010).

[73] U. Wolff, Collective Monte Carlo updating for spin systems, Phys. Rev. Lett. **62**, 361 (1989).

[74] Z. Zhang, J. Shang, C. Jiang, A. Rasmita, W. Gao, and T. Yu, Direct photoluminescence probing of ferromagnetism in monolayer two-dimensional $CrBr_3$, Nano Lett. **19**, 3138 (2019).

[75] R. Dong, Z. Zhang, D. C. Tranca, S. Zhou, M. Wang, P. Adler, Z. Liao, F. Liu, Y. Sun, and W. Shi, A coronene-based semiconducting two-dimensional metal-organic framework with ferromagnetic behavior, Nat. Commun. **9**, 2637 (2018).

[76] T. R. Umbach, M. Bernien, C. F. Hermanns, A. Krüger, V. Sessi, I. Fernandez-Torrente, P. Stoll, J. I. Pascual, K. J. Franke, and W. Kuch, Ferromagnetic coupling of mononuclear fe centers in a self-assembled metal-organic network on Au(111), Phys. Rev. Lett. **109**, 267207 (2012).

[77] L. Šmejkal, J. Sinova, and T. Jungwirth, Emerging research landscape of altermagnetism, Phys. Rev. X **12**, 040501 (2022).

[78] D. J. Thouless, M. Kohmoto, M. P. Nightingale, and M. denNijs, Quantized hall conductance in a two-dimensional periodic potential, Phys. Rev. Lett. **49**, 405 (1982).

[79] S. Takagi, A. Toriumi, M. Iwase, and H. Tango, On the universality of inversion layer mobility in Si MOSFET's: Part II-effects of surface orientation, IEEE Trans. Electron Devices **41**, 2363 (1994).

[80] S. Bruzzone and G. Fiori, Ab-initio simulations of deformation potentials and electron mobility in chemically modified graphene and two-dimensional hexagonal boron-nitride, Appl. Phys. Lett. **99**, 222108 (2011).

[81] B. Radisavljevic, A. Radenovic, J. Brivio, V. Giacometti, and A. Kis, Single-layer MoS_2 transistors, Nat. Nanotechnol. **6**, 147 (2011).

[82] J. Qiao, X. Kong, Z. X. Hu, F. Yang, and W. Ji, High-mobility transport anisotropy and linear dichroism in few-layer black phosphorus, Nat. Commun. **5**, 4475 (2014).

[83] Z. Liu, F. Liu, and Y. S. Wu, Exotic electronic states in the world of flat bands: From theory to material, Chin. Phys. B **23**, 077308 (2014).

[84] D. V. Rybkovskiy, A. V. Osadchy, and E. D. Obraztsova, Transition from parabolic to ring-shaped valence band maximum in few-layer GaS, GaSe, and InSe, Phys. Rev. B **90**, 235302 (2014).

[85] S. Saxena, P. Agarwal, K. Ahilan, F. Grosche, R. Haselwimmer, M. Steiner, E. Pugh, I. Walker, S. Julian, and P. Monthoux, Superconductivity on the border of itinerant-electron ferromagnetism in UGe_2, Nature (London) **406**, 587 (2000).

[86] D. Aoki, K. Ishida, and J. Flouquet, Review of U-based ferromagnetic superconductors: Comparison between UGe_2, URhGe and UCoGe, J. Phys. Soc. Jpn. **88**, 022001 (2019).

[87] C. C. J. Roothaan, New developments in molecular orbital theory, Rev. Mod. Phys. **23**, 69 (1951).

[88] C. Goringe, D. Bowler, and E. Hernandez, Tight-binding modelling of materials, Rep. Prog. Phys. **60**, 1447 (1997).

[89] Z. Zhang, Z. M. Yu, G. B. Liu, and Y. Yao, Magnetictb: A package for tight-binding model of magnetic and nonmagnetic materials, Comput. Phys. Commun. **270**, 108153 (2022).

[90] J. E. Dennis and J. J. Moré, Quasi-newton methods, motivation and theory, SIAM Rev. **19**, 46 (1977).

[91] S. B. Desai, G. Seol, J. S. Kang, F. H, C. Battaglia, R. Kapadia, J. W. Ager, J. Guo, and A. Javey, Strain-induced indirect to direct bandgap transition in multilayer WSe_2, Nano Lett. **14**, 4592 (2014).

[92] L. Li, E. O'farrell, K. Loh, G. Eda, B. Özyilmaz, and A. Castro Neto, Controlling many-body states by the electric-field effect in a two-dimensional material, Nature (London) **529**, 185 (2016).

[93] J. Ye, M. F. Craciun, M. Koshino, S. Russo, S. Inoue, H. Yuan, H. Shimotani, A. F. Morpurgo, and Y. Iwasa, Accessing the transport properties of graphene and its multilayers at high carrier density, Proc. Natl. Acad. Sci. USA **108**, 13002 (2011).

[94] M. Ryazanov, R. K. Kremer, A. Simon, and H. Mattausch, Metal-nonmetal transition and colossal negative magnetoresistance in the gadolinium hydride halides $GdIH_x$ ($0.67 < x < 1.0$), Phys. Rev. B **73**, 035114 (2006).

[95] H. Mattausch, W. Schramm, R. Eger, and A. Simon, Metall-reiche Gadolinium hydrid halogenide, Z. Anorg. Allg. Chem. **530**, 43 (1985).

[96] A. Simon, H. J. Mattausch, G. J. Miller, W. Bauhofer, and R. K. Kremer, *Metal-rich Halides: Structure, Bonding and Properties* (Elsevier, Amsterdam, 1991), Chap. 100, pp. 191–285.

[97] T. Björkman, A. Gulans, A. V. Krasheninnikov, and R. M. Nieminen, Van der waals bonding in layered compounds from advanced density-functional first-principles calculations, Phys. Rev. Lett. **108**, 235502 (2012).